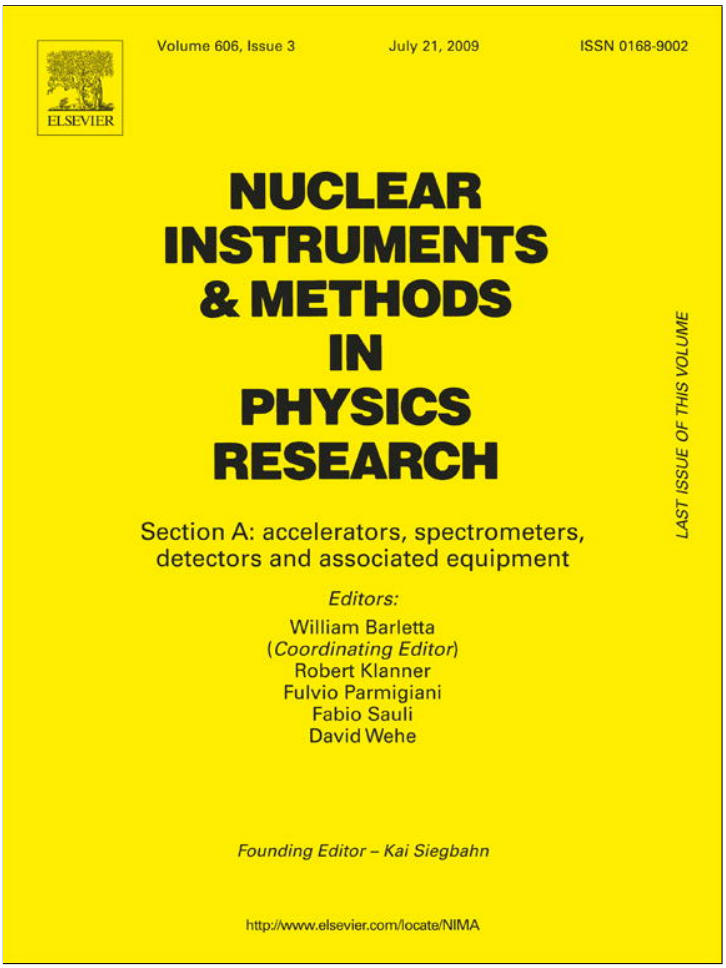

Nuclear Instruments and Methods in Physics Research A 606 (2009) 449–465

Contents lists available at ScienceDirect

Nuclear Instruments and Methods in Physics Research A

journal homepage: www.elsevier.com/locate/nima

Measurement of the background in the NEMO 3 double beta decay experiment

J. Argyriades [a], R. Arnold [b], C. Augier [a], J. Baker [c], A.S. Barabash [d], M. Bongrand [a], G. Broudin-Bay [a], V.B. Brudanin [g], A.J. Caffrey [c], A. Chapon [l], E. Chauveau [e,f], Z. Daraktchieva [j], D. Durand [l], V.G. Egorov [g], N. Fatemi-Ghomi [h], R. Flack [j], A. Freshville [j], B. Guillon [l], Ph. Hubert [e,f], S. Jullian [a], M. Kauer [j], S. King [j], O.I. Kochetov [g], S.I. Konovalov [d], V.E. Kovalenko [b,g], D. Lalanne [a], K. Lang [k], Y. Lemière [l], G. Lutter [e,f], F. Mamedov [i], Ch. Marquet [e,f], J. Martin-Albo [n], F. Mauger [l], A. Nachab [e,f], I. Nasteva [h], I.B. Nemchenok [g], C.H. Nguyen [e,f,t], F. Nova [m], P. Novella [n], H. Ohsumi [o], R.B. Pahlka [k], F. Perrot [e,f], F. Piquemal [e,f], J.L. Reyss [p], J.S. Ricol [e,f], R. Saakyan [j], X. Sarazin [a], L. Simard [a], Yu.A. Shitov [g], A.A. Smolnikov [g], S. Snow [h], S. Söldner-Rembold [h], I. Štekl [i], C.S. Sutton [q], G. Szklarz [a], J. Thomas [j], V.V. Timkin [g], V.I. Tretyak [b,g,*], Vl.I. Tretyak [s], V.I. Umatov [d], L. Vála [i], I.A. Vanyushin [d], V.A. Vasiliev [j], V. Vorobel [r], Ts. Vylov [g]

[a] LAL, Université Paris-Sud, CNRS/IN2P3, F-91405 Orsay, France
[b] IPHC, Université de Strasbourg, CNRS/IN2P3, F-67037 Strasbourg, France
[c] INL, Idaho Falls, ID 83415, USA
[d] Institute of Theoretical and Experimental Physics, 117259 Moscow, Russia
[e] Université de Bordeaux, Centre d'Etudes Nucléaires de Bordeaux Gradignan, UMR 5797, F-33175 Gradignan, France
[f] CNRS/IN2P3, Centre d'Etudes Nucléaires de Bordeaux Gradignan, UMR 5797, F-33175 Gradignan, France
[g] Joint Institute for Nuclear Research, 141980 Dubna, Russia
[h] University of Manchester, M13 9PL Manchester, UK
[i] IEAP, Czech Technical University in Prague, CZ-12800 Prague, Czech Republic
[j] University College London, WC1E 6BT London, UK
[k] University of Texas at Austin, Austin, TX 78712-0264, USA
[l] LPC Caen, ENSICAEN, Université de Caen, CNRS/IN2P3, F-14032 Caen, France
[m] Universitat Autònoma de Barcelona, Spain
[n] IFIC, CSIS - Universidad de Valencia, Valencia, Spain
[o] Saga University, Saga 840-8502, Japan
[p] LSCE, CNRS, F-91190 Gif-sur-Yvette, France
[q] MHC, South Hadley, Massachusetts, MA 01075, USA
[r] Charles University in Prague, Faculty of Mathematics and Physics, CZ-12116 Prague, Czech Republic
[s] INR, MSP 03680 Kyiv, Ukraine
[t] Hanoi University of Sciences, Hanoi, Vietnam

NEMO Collaboration

ARTICLE INFO

Article history:
Received 21 March 2009
Accepted 13 April 2009
Available online 22 April 2009

Keywords:
Double beta decay
NEMO
Background
Radon
Low radioactivity

ABSTRACT

In the double beta decay experiment NEMO 3 a precise knowledge of the background in the signal region is of outstanding importance. This article presents the methods used in NEMO 3 to evaluate the backgrounds resulting from most if not all possible origins. It also illustrates the power of the combined tracking-calorimetry technique used in the experiment.

* Corresponding author at: IPHC, Université de Strasbourg, CNRS/IN2P3, F-67037 Strasbourg, France.
E-mail address: tretyak@jinr.ru (V.I. Tretyak).

0168-9002/$ - see front matter © 2009 Elsevier B.V. All rights reserved.
doi:10.1016/j.nima.2009.04.011

1. Introduction

NEMO 3 is a currently running experiment located in the Laboratoire Souterrain de Modane (LSM) searching for neutrinoless double beta decay ($\beta\beta0\nu$). This decay is a uniquely sensitive probe of the mass and charge conjugation properties of the neutrino. Should it be observed, it would demonstrate that at least one neutrino is a massive Majorana particle. NEMO 3 is also able to detect the rare second order weak double beta decay with its two accompanying neutrinos ($\beta\beta2\nu$), as well as the non-standard neutrinoless decay with Majoron emission ($\beta\beta\chi$). The three decay modes are distinguishable experimentally by the energy sum distribution of the two beta particles. Although the observation of neutrinoless double beta decay is the goal of NEMO 3, its aim is also to measure (or give limits on) half-lives of the other double beta decay processes.

The NEMO 3 detector provides the direct detection of two electrons from the decay by the use of a tracking device and a calorimeter (see Fig. 1). It has three integrated components:

- a foil consisting of different sources of double beta emitters {^{100}Mo (6914 g), ^{82}Se (932 g), ^{116}Cd (405 g), ^{130}Te (454 g), natural Te (614 g of TeO_2), ^{150}Nd (37 g), ^{96}Zr (9 g), ^{48}Ca (7 g)} and pure copper (621 g);
- a tracking volume based on open Geiger cells;
- a calorimeter made of plastic scintillator blocks with photomultiplier tubes.

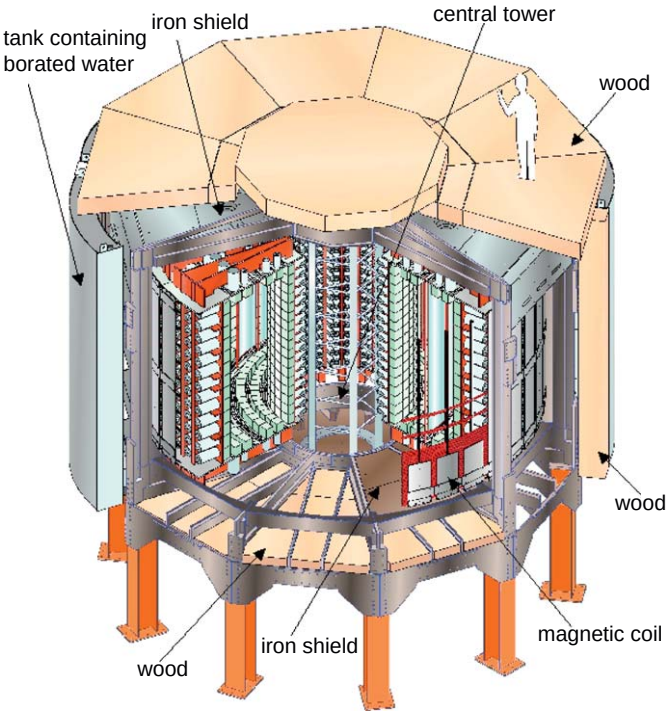

Fig. 1. Schematical view of the NEMO 3 detector.

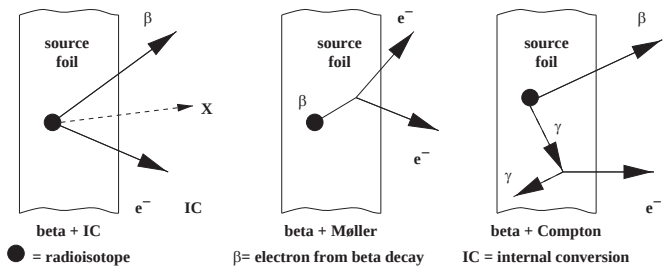

Fig. 2. Internal background production in the source foil.

A magnetic field created by a solenoidal coil surrounding the detector provides identification of electrons by the curvature of their tracks. Besides the electron and photon identification, the calorimeter measures the energy and the arrival time of these particles while the tracking chamber can measure the time of delayed tracks associated with the initial event for up to 700 μs. A full description of the NEMO 3 detector and its performance can be found in [1]. The first results were published in [2–4].

The most significant concern in double beta decay experiments is the background. Although the candidates for double beta decay are selected as events with two electron ($2e^-$) tracks with a common origin on the source foil, there are certain non $\beta\beta$ processes that can mimic the $2e^-$ topology. According to its origin, the background in NEMO 3 is divided into two categories:

- the "internal background" having its origin inside the double beta decay source foil;
- the "external background" coming from all radioactive sources located outside of the foil.

The "internal background" is mainly due to the presence of radioactive isotopes from the ^{238}U and ^{232}Th decay chains. The dominant mechanisms leading to the $2e^-$ topology are (see Fig. 2)

- β decay accompanied by an internal conversion;
- β decay followed by Møller scattering;
- β–γ cascades in which a γ-ray undergoes Compton scattering.

The first mechanism is the dominant one. Particularly troublesome are the isotopes with large Q_β values such as ^{208}Tl ($Q_\beta = 4.99$ MeV) and ^{214}Bi ($Q_\beta = 3.27$ MeV). Fortunately, for these isotopes there are good estimates of the activities obtained from identifiable topologies ($e\alpha$ for ^{214}Bi, $e\gamma\gamma$ and $e\gamma\gamma\gamma$ for ^{208}Tl).

Great care was taken in the production and subsequent purification of the enriched materials, as well as during the source foil production and the mounting of foils in the detector so as to keep any contamination to a minimum given the strict radioactivity limits.

In the region where a signal of neutrinoless $\beta\beta$ decay is expected, the allowed $\beta\beta2\nu$ decay can be an important fraction of the background. Its contribution depends upon the $\beta\beta2\nu$ half-life and the energy resolution of the detector. It is therefore important to carefully study the background in a large energy region where the $\beta\beta2\nu$ decay takes place in order to obtain a good measurement of the half-life of this process.

A component of the external background producing events similar to the internal background is caused by the presence of radon and thoron inside the detector. These elements are highly diffusive radioactive gases. They are outgased in the air from the rock walls of the experimental hall and can enter the detector either through tiny gaps between sectors or through gas pipe joints. The progeny of radon and thoron produces γ-rays and β-decays accompanied by internal conversion (IC), Møller or Compton scattering. If such an event occurs on or near a foil and appears with a $2e^-$ topology it becomes indistinguishable from a double beta decay candidate.

Another component of this background is due to external γ-rays interacting inside the foil. These γ-rays are of different origins:

- γ-rays inside the laboratory, mostly coming from the rock walls;

- neutron interactions in the shield and material of the detector;
- radioactive isotopes present in the detector materials despite the rigorous selection done during the detector construction;
- presence of radon in the air surrounding the detector.

The interaction of γ-rays in the foil can appear like $2e^-$ events by e^+e^- pair creation with misidentification of the charge, double Compton scattering or Compton scattering followed by Møller scattering (see Fig. 3).

In this article the methods used to evaluate the various backgrounds are presented. The very pure copper foils (OFHC) are used to prove their validity. The experimental data of the NEMO 3 detector were used to perform the background measurements.

2. Natural radioactivity inside the tracking volume

2.1. ^{222}Rn *measurement inside the tracking chamber*

The most bothersome external background comes from radon. As shown in Fig. 4, ^{214}Bi is one of the descendants of ^{222}Rn. The β^-decay of ^{214}Bi to ^{214}Po is generally accompanied by several photons which can mimic a $\beta\beta0\nu$ event given its large Q_β value. The ^{214}Po has a half-life of 164 μs and it disintegrates to ^{210}Pb via α-decay.

The ejected alpha particle from the decay of ^{222}Rn can free several electrons from the ^{218}Po atom transforming it to a positively charged ion. Diffusing through the gas of the tracking chamber this ion may be neutralized by different processes, such as recombining with negative ions in the gas, a charge transfer by neutral molecules with a small ionization potential or the capture of an electron created during the gas discharge near the open Geiger cell wires [6,7]. It is difficult to predict the proportions of neutral and charged atoms of ^{218}Po in the gas of the NEMO 3 tracking chamber. However, following some earlier studies [8–10] one can suppose that the proportion of neutral atoms of ^{218}Po which are in the gas is small and that the majority of the charged ^{218}Po is deposited on the surfaces of the cathode wires of the Geiger cells. Here the measurement of the radon activity in the tracking chamber is done under the assumption that the descendants of ^{222}Rn are deposited on the wires. It should be noted that the final background resulting from the presence of ^{222}Rn does not depend critically upon this assumption. If one supposes that the descendants of this gas are uniformly distributed in the tracking chamber the background estimation remains unchanged within the errors. A possible deposition on the foil surfaces is also taken into account in the analysis performed to measure internal foil contamination by ^{214}Bi (see Section 4).

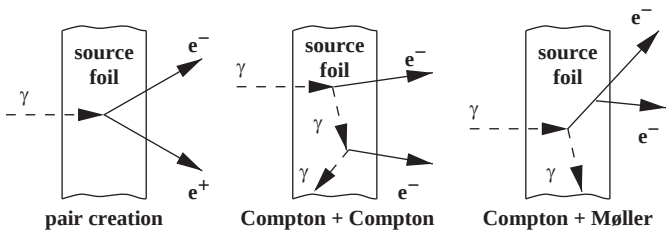

Fig. 3. External background production in the source foil.

2.1.1. Event selection

In the NEMO 3 experiment, the data acquisition allows one to readout signals from delayed tracks in order to tag the α-particles from ^{214}Po decays associated with electrons from ^{214}Bi decays. The ^{214}Bi decays followed by ^{214}Po decays (hereafter referred to as BiPo events) are used for the measurement of the radon activity. Typical examples of such events with detected electron and α-particle tracks are shown in Fig. 5. Two types of spurious events can appear in a sample of BiPo candidates. They are due to:

- Random coincidence of two independent events closely localized in space and occurring inside the 700 μs time window. The delay time distribution is flat in this case.
- A single event accompanied by one or more delayed signals caused by refiring of neighboring Geiger cells. The number of

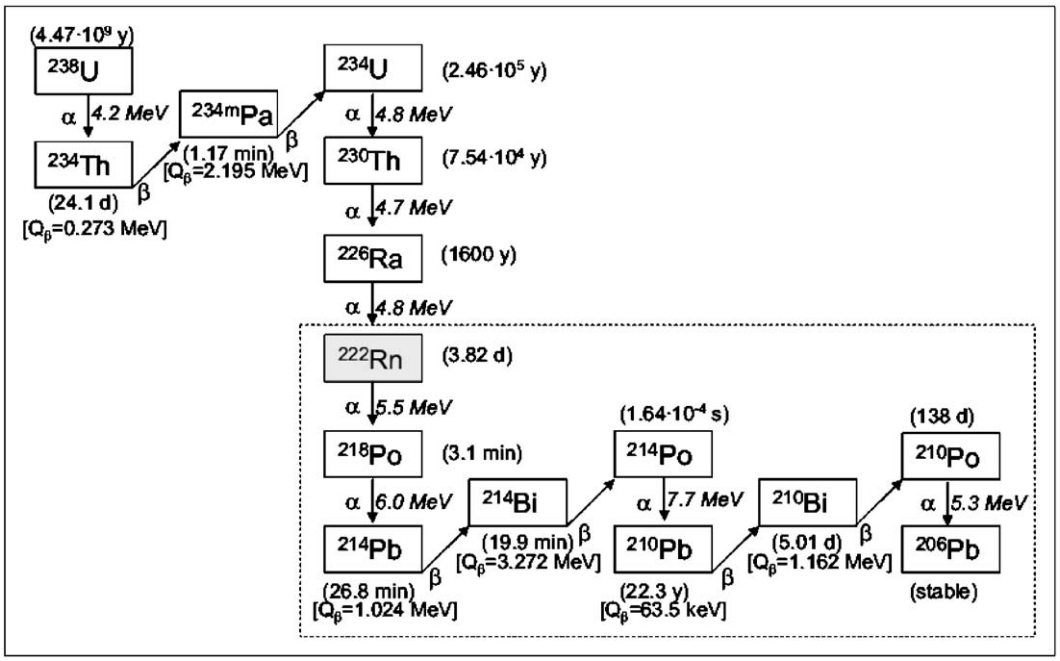

Fig. 4. Decay chain of the radioactive family of ^{238}U. The half-lives and decay energies are taken from Ref. [5].

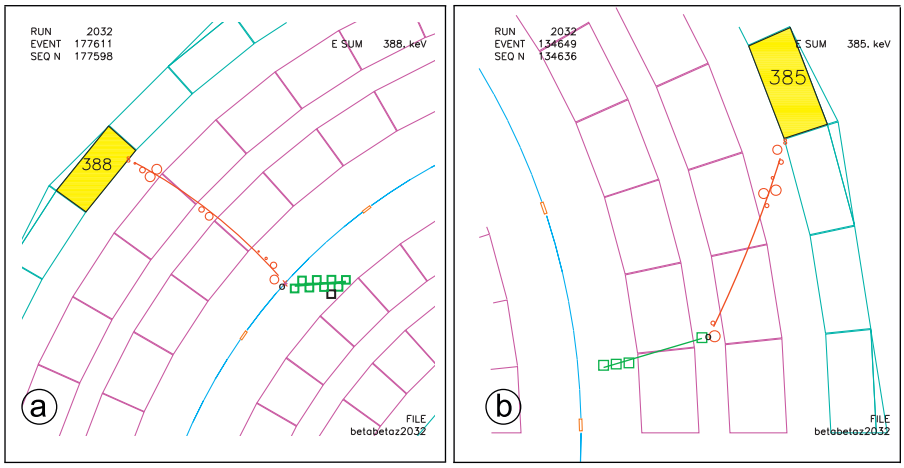

Fig. 5. Examples of BiPo event candidates, viewed from the top. In each event the prompt track is shown in red (electron), delayed track—in green (α-particle). The two tracks have a common vertex: (a) on the source foil, (b) inside the tracking volume. Scintillator blocks located at top and bottom (wall) are shown as magenta (blue) boxes.

this kind of event decreases sharply with the delay time, so their distribution is nearly exponential.

In order to reduce the contribution from refirings, the following cuts are applied:

- for events with only one delayed signal, the delay must be greater than 90 μs;
- for events with more than one delayed signal, the delay must be greater than 30 μs.

It is required that the delayed signals have to be located close to the "prompt" (i.e. electron) track or to the event vertex on the source foil. The group of selected delayed signals must be within 2.1 μs (corresponding to the maximum transversal drift time in the Geiger cells) and follow a straight line in space in order to exclude random coincidences of delayed events of different origins. In the tracking chamber the maximum range of the 7.7 MeV α-particle emitted by ^{214}Po is 36 cm. This value is also taken into account in the selection of events.

Applying these criteria the mean efficiency to select a BiPo event produced on a wire surface has been estimated by a Monte Carlo (MC) simulation to be 16.5%. In this work all simulations [11] are based on GEANT3 [12] using DECAY0 [13] as event generator.

The time distribution of the delayed tracks (see Fig. 6) provides an efficient way to validate the quality of the event selection. The fit to the distributions allows the half-life of ^{214}Po to be evaluated. The proportions of events due to refirings and random coincidences are also determined from the fit. They are found to be negligibly small with $0.6 \pm 1.3\%$ for the single delayed signal and $1.9 \pm 0.8\%$ for the multiple delayed signals as shown in Fig. 6. In spite of the systematic uncertainty of ~1 μs on the result, the half-life of ^{214}Po for the single delayed signal events is $T_{1/2}(^{214}\text{Po}) = 162.9 \pm 0.2(\text{stat.only})$ μs and for the multiple delayed signal events is $T_{1/2}(^{214}\text{Po}) = 161.9 \pm 0.8(\text{stat.only})$ μs, a comparison with the table value of $T_{1/2}(^{214}\text{Po}) = 164.3 \pm 2.0$ μs [14] confirms that the delayed tracks are due to the α-particles of ^{214}Po.

2.1.2. ^{222}Rn *monitoring*

Using the method described in Section 2.1.1 the mean ^{222}Rn level in the tracking volume was analyzed. The results of the radon monitoring are shown in Fig. 7.

In order to decrease the level of ^{222}Rn, a radon reduction factory has been installed in the underground laboratory to inject nearly radon free air into a tent built around the detector. It became operational at the beginning of October 2004. Therefore, the NEMO 3 data have been divided into two parts according to the collection dates. The first part of the data corresponds to acquisition done from the beginning of the experiment in February 2003 up to the end of September 2004 ("Phase 1"). The second part of the data presented here includes the runs from October 2004 up to the end of 2006 ("Phase 2"). Data collection continues under the conditions of Phase 2. The mean ^{222}Rn level was measured to be 37.7 ± 0.1 mBq/m^3 for Phase 1 and 6.46 ± 0.02 mBq/m^3 for Phase 2 inside the tracking volume (only statistical errors are given).

According to the goal of the analysis the ^{222}Rn monitoring provides the possibility to select data with different radon levels.

2.1.3. *Spatial distribution of the* ^{214}Bi

In the preceding paragraph the results of the mean ^{214}Bi activity measurements in the tracking volume were given. For double beta decay studies it is important to know the ^{214}Bi distribution close to the source foils.

The starting point of the electron track closest to the delayed track is used to localize the decay point of a BiPo event. The position of such a point is defined by the Geiger cell layer number, running from 08 to 00 for the inner Geiger cell layers and from 10 to 18 for the outer Geiger cell layers (Fig. 8). The vertical position is the measured Z coordinate[1] of the electron's origin. Its azimuthal position is given by the sector number from 0 to 19.

The ^{214}Bi distribution inside the tracking chamber for Phase 1 and Phase 2 is shown in Fig. 9. For both phases there is a consistent pattern that is scaled to the radon activity. Greater activity is observed in layers 03–06 and 13–16 and is explained by the large gap between Geiger layers 03–04, 13–14, 05–06 and 15–16 (Fig. 8).

In order to detect possible sources of ^{222}Rn outgasing or ^{214}Bi pollution, the spatial distribution of ^{214}Bi in Phase 2 has been compared with Phase 1. The results are shown in Fig. 10 and indicate that the distributions of ^{214}Bi for the two phases are similar in the whole tracking volume except at the borders. There is a residual ^{214}Bi activity near the scintillator walls and end caps. The enhanced ^{214}Bi activity near the foil extremities (especially in

[1] Origin $Z = 0$ is in the middle plane of the detector.

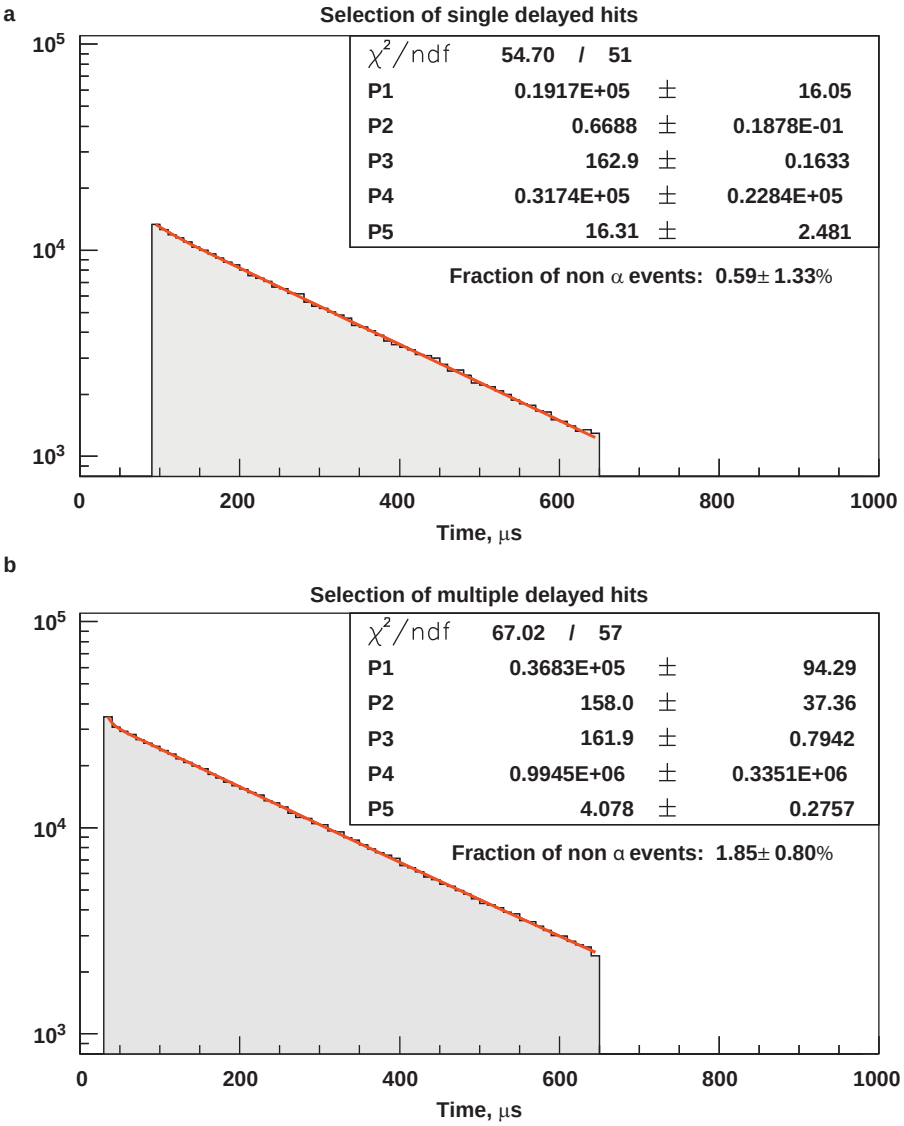

Fig. 6. The time distributions of events selected with (a) single and (b) multiple delayed signals. Each distribution was fit to the function: $f(time) = P1e^{-time/P3/\ln 2} + P2 + P4e^{-time/P5/\ln 2}$ where $P1$ and $P4$ are scaling constants, $P2$ is the amplitude of random coincidences, $P3$ the ^{214}Po half-life in μs and $P5$ the time constant of the refirings.

sector 3 with molybdenum foils) probably originates from the foil holders and/or the scintillator surfaces. In order to exclude top and bottom parts with the "extra" ^{214}Bi activity, only events with vertices of $|Z| < 120$ cm are taken into account in the following.

In the ββ analysis most of the background due to ^{222}Rn appears to come from the regions close to the source foils. Therefore, the observed non-uniformity of ^{214}Bi distribution along the vertical direction for distant Geiger cell layers is neglected. While the variations in the azimuthal direction from sector-to-sector are accounted for. The mean activities measured for each sector layer-by-layer are used. The test of the background model (see Section 5) is performed with copper foils located in sector 0. For this sector the results of the ^{214}Bi activity measurements for the layers closest to the foil are given in Table 1.

2.1.4. ^{222}Rn *activity measurement using* eγ *events*

It is also possible to detect ^{214}Bi using eγ events. A large fraction of the ^{214}Bi decays is accompanied by a high energy γ-ray. However, the eγ events are contaminated by external γ-rays which Compton scatter on the wires of the Geiger cells (see Section 3).

To suppress this background contribution, only events with a γ-ray of energy greater than 1 MeV are used. In order to select events originating from the tracking volume and not from the source foils, only electrons with their starting point on the Geiger cell layers 01, 11, 02 and 12 are analyzed. The results for the mean ^{214}Bi activity for the second and third Geiger cell layers using eα and eγ topologies are presented in Table 2.

The method involving eγ events has a larger background with approximately three times smaller detection efficiency compared to the method using the delayed tracks. However, the eγ events allows one to address the measurements of delayed tracks and to estimate the systematic error on ^{222}Rn activity inside the tracking chamber to within 10%.

2.2. ^{220}Rn (^{208}Tl) *activity measurements inside the tracking chamber*

If ^{220}Rn is present in the gas of the tracking chamber, it constitutes a source of ^{208}Tl. Given the high Q_β value, ^{208}Tl is a serious concern for neutrinoless double beta decay search. The beta decay of ^{208}Tl is almost always accompanied by a γ-ray of

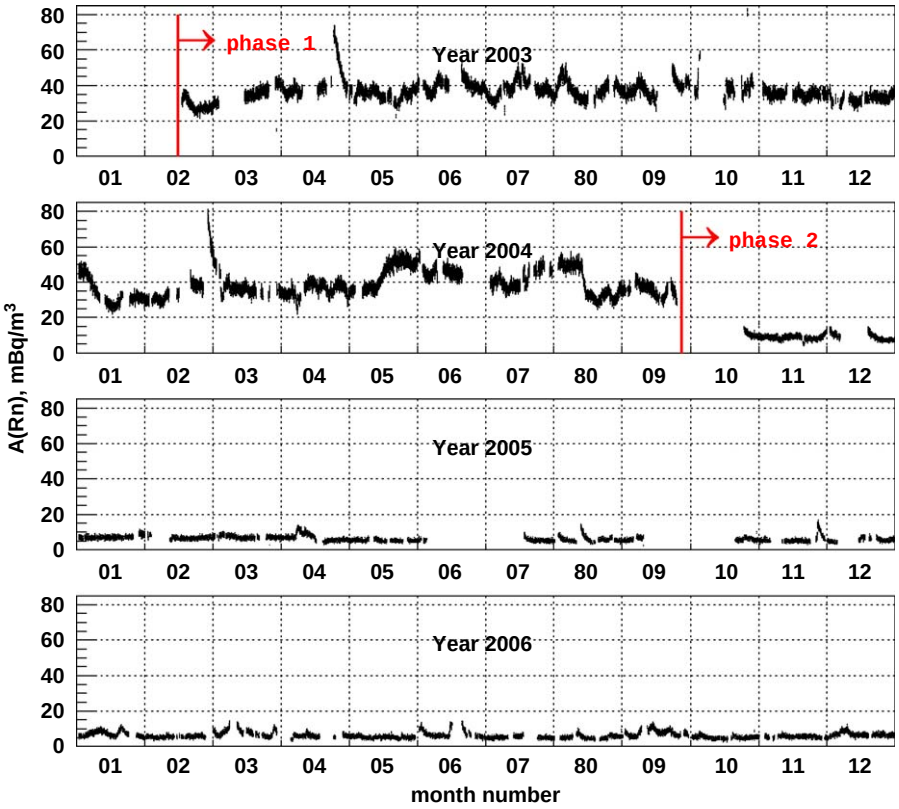

Fig. 7. The ^{222}Rn activity in mBq/m^3 inside the tracking chamber measured on an hourly basis.

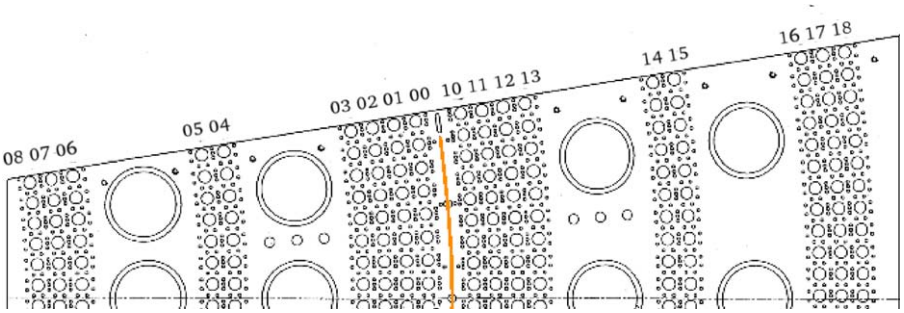

Fig. 8. Lay out of the end-cap showing the Geiger cell layer configuration, top view. The inner layers are numerated 00–08 starting from the source foil located in the center. The outer layers are 10–18 as indicated.

2615 keV from the first excited state of ^{208}Pb [5]. In the case of the de-excitation by IC electron emission one can observe two electrons with a total energy of approximately 3 MeV which can mimic ^{100}Mo and ^{82}Se neutrinoless double beta decay. Therefore, the thoron content of the gas mixture has been studied by means of the ^{208}Tl beta decay detection.

2.2.1. Selection criteria

The beta decay of ^{208}Tl is mainly accompanied by two or three γ-rays. Therefore, e$\gamma\gamma$ and e$\gamma\gamma\gamma$ topologies are used in the analysis. The event vertex is defined by the origin of the electron. In order to reject events coming from the source foil only events with vertices on the Geiger cell layers 01–04 and 11–14 are analyzed. Tracks starting in planes 05–08 and 15–18 are too short to allow accurate event selection by time-of-flight.

For both topologies the electron has an energy greater than 200 keV and each γ-ray an energy greater than 150 keV. The time-of-flight method is used to ensure the common origin of all the particles involved. In order to reduce backgrounds the γ-ray with the highest measured energy (E_γ) is required to have $E_\gamma > 1700$ keV and the energy of the electron must satisfy the condition $E_e > (4200 - \sum E_\gamma)$ keV.

2.2.2. Results of the measurement

The data have been analyzed separately for the two phases and the two topologies. The results of the measurements are presented in Table 3. There is good agreement between the results obtained for the e$\gamma\gamma$ and e$\gamma\gamma\gamma$ topologies. The average activities resulting from them are 3.5 ± 0.4 mBq for Phase 1 and 2.9 ± 0.4 mBq for Phase 2. The systematic uncertainty is estimated to be less than 10% and comes mostly from the γ-ray detection efficiency. A comparison of the results for the two phases shows no strong difference due to the detector environment but indicates a possible weak outgasing of thoron inside the tracking volume. Taking into account the 35.94% branching fraction of ^{208}Tl in the ^{232}Th chain, the measured ^{208}Tl activity of $\sim$3 mBq corresponds to $\sim$8 mBq of ^{220}Rn. MC simulations show that this low level of thoron inside the tracking device is much

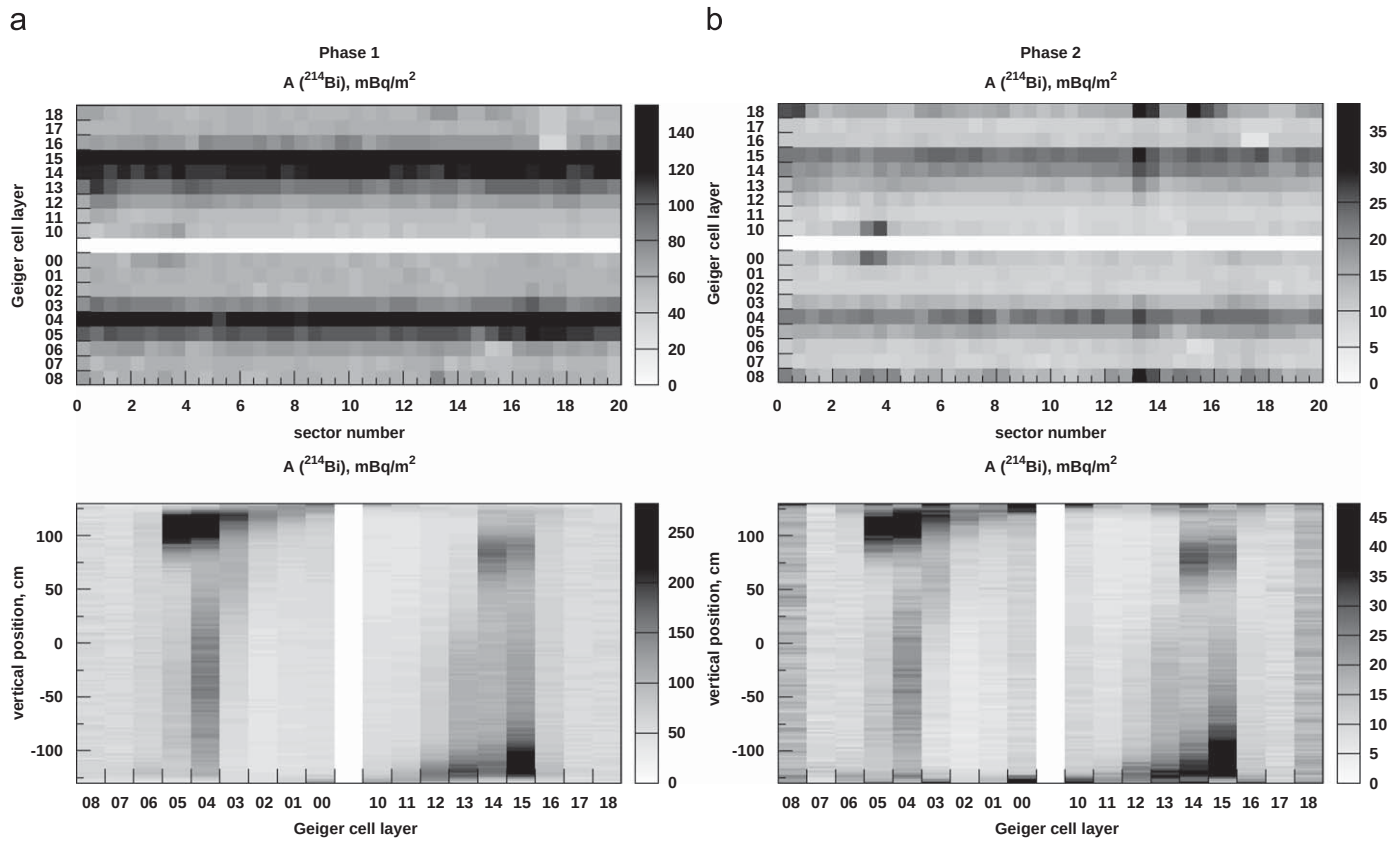

Fig. 9. Plots of the ^{214}Bi activity as a function of Geiger cell layer, sector number and vertical position inside the tracking chamber for data of (a) Phase 1 and (b) Phase 2.

less of a concern for neutrinoless double beta decay than the presence of radon. For both phases the background from thoron in the $2e^-$ channel is more than one order of magnitude lower than the background originating from radon.

2.3. ^{210}Pb (^{210}Bi) activity inside the tracking chamber

One probable source of background with its origin on the Geiger cell wires is the β-decay of ^{210}Bi from ^{210}Pb ($T_{1/2} = 22.3$ y) in the ^{238}U decay chain (see Fig. 4). Given its Q_β of 1.16 MeV, this radioactive isotope is of no concern for this neutrinoless double beta decay search, but it must be considered in the precise measurement of the two neutrino double beta decay spectra.

One electron events with an energy greater than 600 keV and their vertices associated with Geiger cells are selected to measure the ^{210}Bi activity on the wire surfaces. The results for both phases are in Fig. 11 and Table 4.

Approximately the same activity values and spatial distribution are measured in both data samples, while a large variation of ^{210}Bi activity from one sector to another is observed. The origin of the non-uniformity in ^{210}Pb deposition on the wires is most probably due to the different histories of the wires and conditions during the wiring of the sectors.

3. External γ-ray flux

The external γ-ray flux is one of the sources of $2e^-$ events and therefore a background for double beta decay. With the NEMO 3 data it is possible to measure this flux using the events resulting from single or double Compton scattering.

If an incoming γ-ray undergoes Compton scattering inside a scintillator block leaving the scattered electron unseen in the tracking chamber and subsequently rescatters in the foil ejecting an electron which hits a scintillator block, an event of eγ topology is observed, see Fig. 12a. Such an event from a double Compton scattering is identified as an "eγ-external" event as opposed to an "eγ-internal" event with both particles coming from a decay or an interaction produced inside the foil. Using time-of-flight measurements and the timing properties of the detector it is easy to distinguish an eγ-external event from an eγ-internal event.

When a single Compton scattering of the incoming γ-ray occurs very close to the surface of the scintillator block, the scattered electron, provided it has sufficient energy, crosses the tracking chamber. The topology of such an event is a pair of tracks of opposite curvature sign coming from the foil. Using the track curvatures and time-of-flight information it is easy to select such "crossing electron" events, see Fig. 12b. A possible background for this type of event is from β-emitters at the detector's inner surface.

3.1. γ-ray flux from surrounding rocks

In the LSM underground laboratory there is a significant flux of γ-rays coming from natural radioactivity in the surrounding rocks. This mostly includes gamma radiation from ^{40}K, ^{214}Bi and ^{208}Tl decays. A passive shield, surrounding the detector, has been constructed to reduce this source of background. The shield consists of low radioactivity iron plates and tanks filled with borated water, see Fig. 1.

The γ-ray energy spectrum in the LSM laboratory has been measured using a NaI detector. In Table 3 of Ref. [15] one can find intensities of the 2.61 and 1.46 MeV γ-ray lines of ^{208}Tl and ^{40}K decays, respectively. The intensities of the lines corresponding to

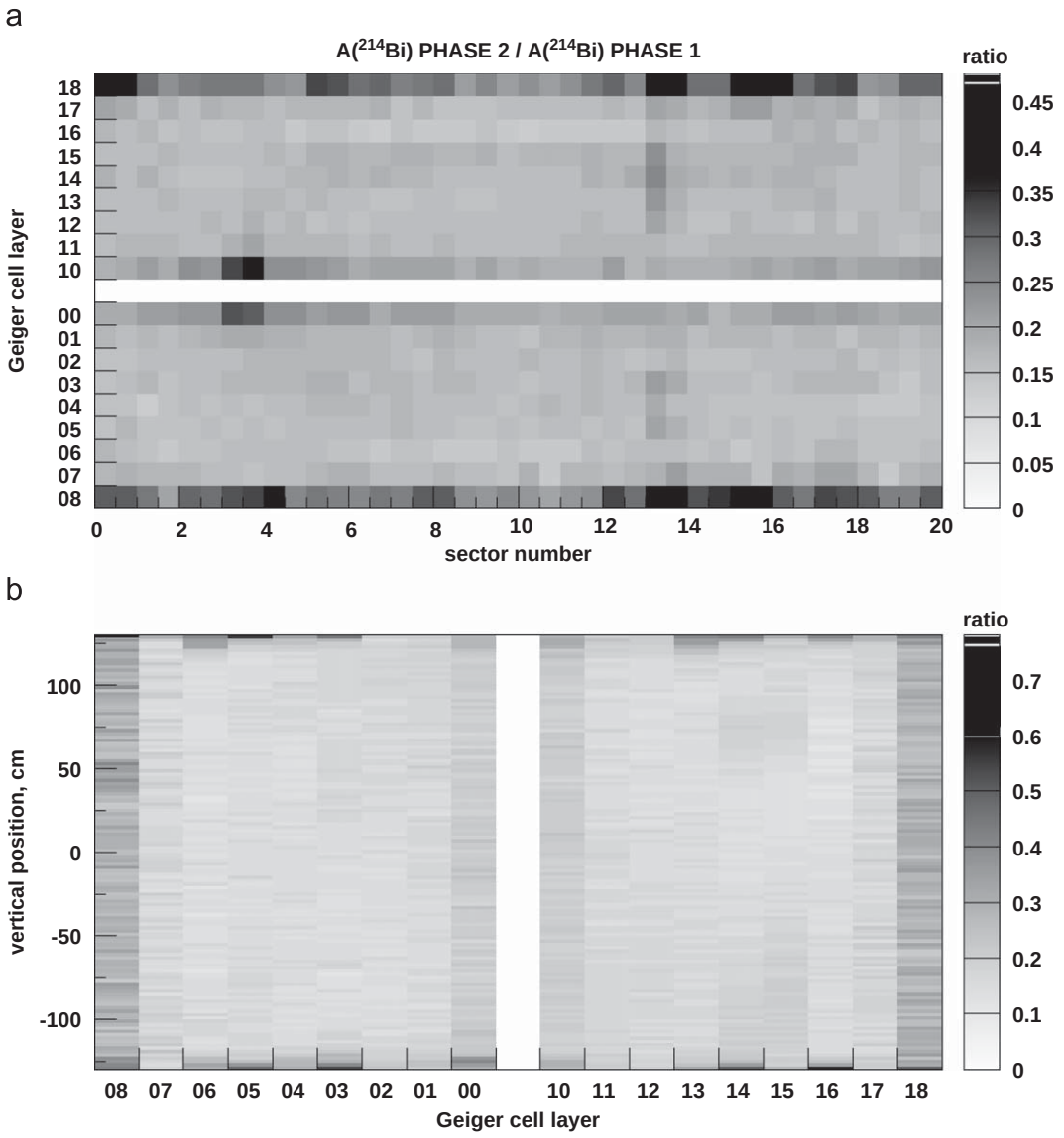

Fig. 10. Ratio of ^{214}Bi activity for two data samples (a) as a function of Geiger cell layer and sector number and (b) vertical position in the Geiger cell layers.

Table 1
The ^{214}Bi activity in mBq for the Geiger cell layer closest to the copper foils of sector 0.

	A(^{214}Bi), mBq	
	Phase 1	Phase 2
Inner foil side, sector 0	724 ± 10	134 ± 4
Outer foil side, sector 0	598 ± 8	101 ± 3
20 sectors average	700 ± 1	140 ± 1

The average activity for the 20 sectors is also presented. Statistical errors are given.

Table 2
Results of the ^{222}Rn measurements on the second and third Geiger cell layers of the tracking chamber using two event topologies are shown.

Geiger cell layer	A(^{214}Bi), mBq			
	02	01	11	12
eα	598 ± 3	701 ± 3	706 ± 3	800 ± 3
eγ	688 ± 7	624 ± 7	645 ± 5	727 ± 6

Statistical errors are given.

^{214}Bi decay have not been evaluated in that work, however, with the published spectrum, one can estimate the strength of the 1.76 MeV γ-ray line and use it as a reference. Relative ratios between different ^{214}Bi lines can be found in an earlier work [16]. Although these measurements were done for the Gran Sasso underground laboratory, one can assume that the rock composition of the two sites is similar, and therefore the attenuation is similar too. The result of this compilation for the γ-ray flux is summarized in Table 5.

In order to evaluate the corresponding background in NEMO 3 a two stage MC simulation has been done. First, a simple MC simulation was performed to estimate the attenuation of the NEMO 3 shielding (iron plates and water tanks) for the spectrum from Table 5. The MC provided energy and angular spectra of the

γ-rays after the shielding with a total attenuation factor of 3.5×10^{-5}.

The energy and angular spectra were then parametrized for a MC simulation with all the components of NEMO 3. This simulation showed that, after cuts were applied, the γ-ray flux from the laboratory accounts for ~2% of the total measured external background, see Fig. 13. Consequently it can be neglected and taken into account by a slight adjustment of other components in the external background model. The most important contribution expected due to the PMT radioactivity measured with the HPGe detectors [1] is also demonstrated in this figure.

3.2. Neutrons

Neutrons can contribute to the external background via the neutron capture process resulting in emission of γ-rays. The neutron flux in the LSM has been measured [17,18] and originates from spontaneous fission and (α,n) reactions due to trace amounts of uranium in the rocks. The NEMO 3 neutron shield thermalizes fast neutrons with energies of a few MeV and suppresses thermal and epithermal neutrons [1].

A series of calibration runs with an AmBe neutron source in the vicinity of the detector has been done to check the shield's efficiency. These runs may also be used to evaluate the neutron background for ββ2ν measurements. The energy sum distribution of crossing electron events for Phase 1 data is shown in Fig. 14. The distribution for a run with the AmBe source is superimposed on it. A pronounced tail at energies up to 8 MeV is seen in both distributions and is a characteristic feature of neutron captures in the detector walls. This tail above 4.5 MeV is used for normalization of the neutron source distribution (Fig. 14). Attributing all the data in this energy region to neutrons one can see that the neutron contribution to the low energy part of the spectrum measured without the AmBe source is very small. In this way one finds that the neutron background can amount to 0.03% of the total at energies below 4 MeV. Therefore, this background can be neglected for ββ2ν analysis.

Table 3
The number of observed events, number of estimated background events, signal efficiency and the results of the measurements of ^{208}Tl activity inside the tracking chamber found for both phases via eγγ and eγγγ topologies.

Topology	N (observed)	N (estimated bgr)	Eff, %	A(^{208}Tl), mBq
Phase 1				
eγγ	342	22.4	0.26	3.5 ± 0.4
eγγγ	63	1.8	0.05	3.3 ± 0.5
Phase 2				
eγγ	322	6.6	0.24	2.8 ± 0.3
eγγγ	79	1.2	0.05	3.5 ± 0.5

3.3. External γ-ray flux model

The principal source of the external background is the natural radioactivity of the detector components. The dominant one is due to the PMTs contamination by ^{226}Ra, ^{228}Ra and ^{40}K as known from the results of HPGe detector measurements [1]. It is addressed in the MC simulation with decays of ^{214}Bi, ^{208}Tl, ^{228}Ac and ^{40}K inside the PMT glass. However, the use of the PMT activities allows one to reproduce roughly only half of the observed experimental eγ-external events, see Fig. 13. The small

Table 4
Activity of ^{210}Bi in Bq on wire surfaces of Geiger cell layers which are next to the foils.

Sector	0	1	2	3	4
Phase 1	6.21 ± 0.37	2.20 ± 0.11	2.95 ± 0.28	3.52 ± 0.21	2.60 ± 0.17
Phase 2	5.83 ± 0.35	2.10 ± 0.12	2.76 ± 0.25	3.31 ± 0.20	2.41 ± 0.13
Sector	5	6	7	8	9
Phase 1	12.62 ± 0.73	3.26 ± 0.17	5.09 ± 0.52	3.29 ± 0.25	1.89 ± 0.24
Phase 2	11.84 ± 0.63	3.17 ± 0.16	4.71 ± 0.42	3.13 ± 0.19	1.85 ± 0.14
Sector	10	11	12	13	14
Phase 1	2.86 ± 0.23	2.10 ± 0.24	4.51 ± 0.49	16.72 ± 0.93	2.21 ± 0.14
Phase 2	2.71 ± 0.18	2.00 ± 0.13	4.28 ± 0.37	17.00 ± 1.16	2.11 ± 0.14
Sector	15	16	17	18	19
Phase 1	12.91 ± 0.70	18.37 ± 0.99	14.48 ± 0.73	2.48 ± 0.12	3.87 ± 0.44
Phase 2	12.17 ± 0.63	17.43 ± 0.93	13.80 ± 0.70	2.40 ± 0.12	3.84 ± 0.41

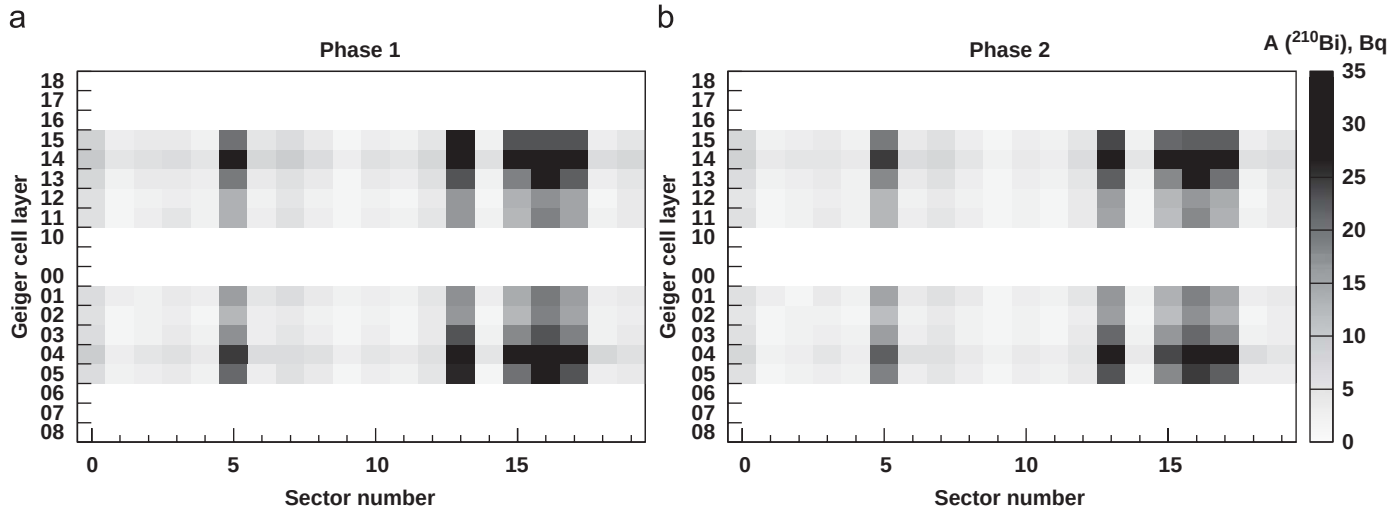

Fig. 11. Plot of ^{210}Bi activity in Bq on the Geiger cell wire surfaces as a function of the event vertex position for (a) Phase 1 and (b) Phase 2.

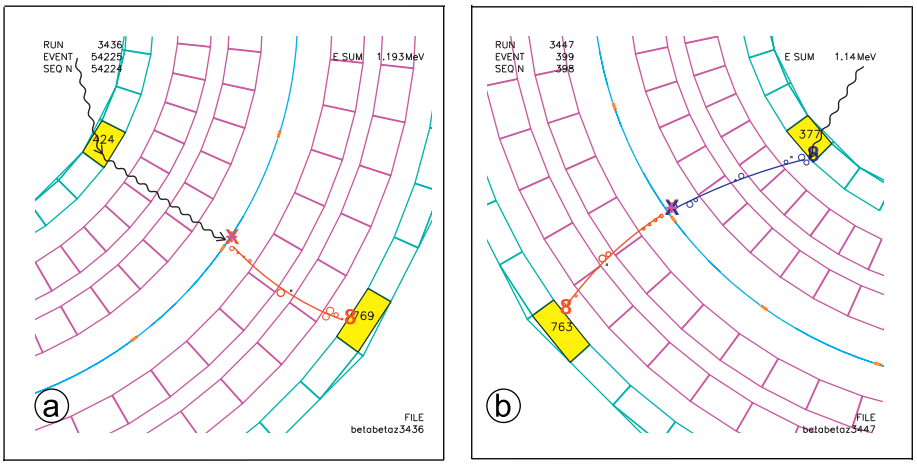

Fig. 12. Examples of (a) eγ-external and (b) crossing electron events. Presumed γ-rays shown by wavy lines are superimposed to the event display.

Table 5
Simplified model of γ-ray flux in the LSM underground laboratory.

Isotope	γ-ray energy, keV	Flux, $cm^{-2}\,s^{-1}$
^{40}K	1461	0.1
^{208}Tl	2615	0.04
^{214}Bi	1764	0.05
	1600	0.026
	1300	0.041
	1120	0.046
	609	0.109
Total		0.411

fraction of each component of NEMO 3 was measured extrapolating the results to the total amount of the material. Therefore, these activities are used as free parameters in order to fit the experimental data. The presence of these isotopes and of ^{60}Co in other parts of the detector have also been taken into account. The list of potential isotopes providing the low energy γ-rays is long. It includes for example ^{54}Mn, ^{58}Co, ^{65}Zn, ^{137}Cs and ^{234m}Pa. In order to take them into account and to improve the description of the low energy part of the gamma spectrum, a flux of 1 MeV γ-rays was simulated at the external surface of the calorimeter.

Not all components of the apparatus or sources of background have been considered so the results of the fit described below should not be interpreted as a measurement of the internal contamination of the corresponding elements of the detector. The purpose of this study is to provide an effective model able to reproduce the external γ-ray flux.

The external background was evaluated using two types of events, eγ-external and crossing electrons. A global fit of the following distributions was performed: the total energy released in the calorimeter, the energy deposited by the electron, the cosine of the angle between the directions of the electron and γ-ray for the eγ-external events, the total energy and finally the energy of the electron after crossing the tracking volume for the crossing electron events. In order to describe the external γ-ray flux coming into the detector in more detail three sets of histograms were produced. These are for the incoming γ-ray signals detected by a counter at the internal wall, external wall and end-caps.

First the external background model parameters are fixed from the Phase 2 data where one can neglect the radon in the air surrounding the detector given its very low level (~0.1 Bq/m^3). The activities of the background model presented in Table 6 and the 1 MeV γ-ray flux of 0.446 $m^{-2}\,s^{-1}$ reflect the data for the incoming γ-rays detected by the calorimeter of NEMO 3. The results of fit are shown in Fig. 15. They demonstrate that the model describes well the γ-ray flux coming through the internal wall (Fig. 15a), through the external wall (Fig. 15b) and from top and bottom (Fig. 15c) as seen with the eγ-external events. The crossing electron channel requires an additional source of electrons that was found to be possible to reproduce with 7.3 mBq/m^2 of ^{234m}Pa and 120 mBq/m^2 of ^{210}Bi on the surface of the scintillator blocks. The distributions for the whole detector are also presented in Fig. 15. In the Fig. 15d one can see the distribution of the total energy measured in the calorimeter for crossing electron events, where the beta emitters provide a noticeable contribution. However, they are negligible in the case of eγ-external events for which one can see the distributions of the energy sum of the electron and γ-ray in Fig. 15e and of the detected electron energy in Fig. 15f.

Then the Phase 1 data were fit with the model including the contribution of radon and thoron in the air thus simulating ^{214}Bi and ^{208}Tl decays in the gapbetween the iron shield and the tracking chamber walls. For radon the activity of 11 Bq/m^3 is obtained in good agreement with the results of the radon monitoring in the LSM. The value of the thoron activity which agrees with the NEMO 3 data is 0.22 Bq/m^3. The mean activity of ^{60}Co for Phase 1 is higher by a factor of 1.3 when compared to Phase 2. This is reasonable considering the ^{60}Co half-life of $T_{1/2} = 5.2$ y. The low-energy γ-ray flux for Phase 1 was found to be twice as high than in Phase 2. As one can see in Fig. 16 the background model fits well the Phase 1 data too.

The total number of crossing electron and eγ-external events and their observed energy distributions are well reproduced for the whole detector. Nevertheless, one may expect that the background may vary from one sector to another due to possible inhomogeneities of the detector materials. The distribution of the number of observed events by sector is not uniform but the pattern is repeated by Monte Carlo calculations, see Fig. 17. It indicates that the non-uniformity is mainly due to the detector's acceptance. A small number of dead PMTs and Geiger cells that vary from sector-to-sector accounts for this. The difference between the number of observed and expected crossing electron and eγ-external events per sector does not exceed 10%.

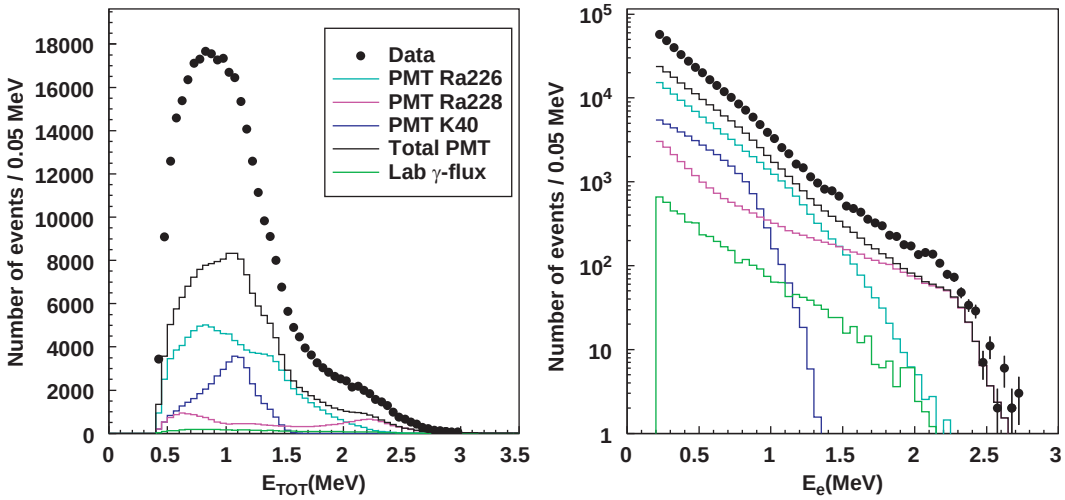

Fig. 13. The sum of the γ-ray and electron energy (E_{TOT}) and the electron energy (E_e) of the eγ-external events in Phase 2 data. The expected contributions due only to the γ-ray flux from the laboratory (see Table 5) and from the photomultiplier tubes are also shown.

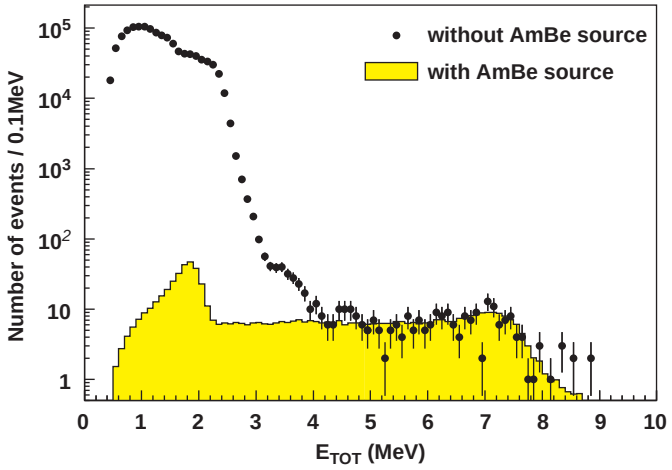

Fig. 14. Energy sum distribution of crossing electron events for 404 days of data (Phase 1). The superimposed histogram represents the distribution obtained for 25 h, of data with an AmBe neutron source and scaled by the factor 6.9×10^{-3}.

Table 6
Components of the external background model.

Components of NEMO 3	Activity (Bq)			
	^{40}K	^{214}Bi	^{208}Tl	^{60}Co
Photomultiplier tubes	1078. ± 32.	324. ± 1.	27.0 ± 0.6	
Plastic scintillators	21.5 ± 0.9			
μ-metal PMT shield				14.6 ± 2.6
Iron petals	100. ± 4.	9.1 ± 1.0	3.1 ± 0.5	6.1 ± 1.8
Copper on petals				47.6 ± 7.8
Internal tower				18.4 ± 0.8
Iron shield		7360. ± 200.	484. ± 24.	

3.4. Test of the model with eeγ-external events

This type of event is similar to the eγ-external one, where an incoming γ-ray deposits some part of its energy in the calorimeter and hits a foil, but here two electrons are emitted from the foil due to double Compton scattering in the foil or due to a Møller scattering of a single Compton electron. The probability for a γ-ray to produce two electrons in the foil is about three orders of magnitude lower than for a single Compton electron. So the statistics for this channel are rather poor. Requiring the γ-ray energy deposit $E_\gamma > 200$ keV the total number of events observed for 969 days of data collection is 420 compared to 409 events expected according to the external background model. The distribution of the energy sum of the two electrons in these events is shown separately for Phase 1 and Phase 2 in Fig. 18. The total number of observed $2e^-$ events produced by detected external γ-rays as well as their energy sum distribution are well reproduced by MC calculations.

4. Radioactivity inside the source foils

4.1. Measurements of the internal ^{214}Bi activity

The internal ^{214}Bi contamination of the source foils is measured with BiPo decays through the detection of eα events. The energy loss of alpha particles in the foil is significantly larger compared to the energy loss in the gas. As a consequence the α-track length depends on the ^{214}Po decay location. Therefore, the delayed track length distribution was used to measure the internal impurities of the source foils.

As in the case of radon activity measurements it is assumed that the ^{214}Bi is deposited on the wire surfaces. The possibility of a deposition on the foil surface is also considered. Phase 2 data is used to minimize the contribution from the radon in the tracking detector. Only events from the source foil (see Fig. 5a) are used. The selected events are divided into four groups according to the delayed track location with respect to the foil (inner or outer side) and to the electron track (on the same side of the foil or on the opposite side).

An example of delayed track length distributions is shown for the selenium foils of the first production,[2] Fig. 19. These are fit with five contributions corresponding to the different locations of the ^{214}Bi. The five are from inside the ββ material, on the two source surfaces and in the wire surfaces on both sides of the foil.

Except for the metallic molybdenum (^{100}Mo(m)) and the copper foils, the NEMO 3 source foils are made of thin mylar films sandwiching the active ββ material. The mylar films are

[2] Selenium foils are from two separate enrichment tasks, which are called ^{82}Se(I) and ^{82}Se(II).

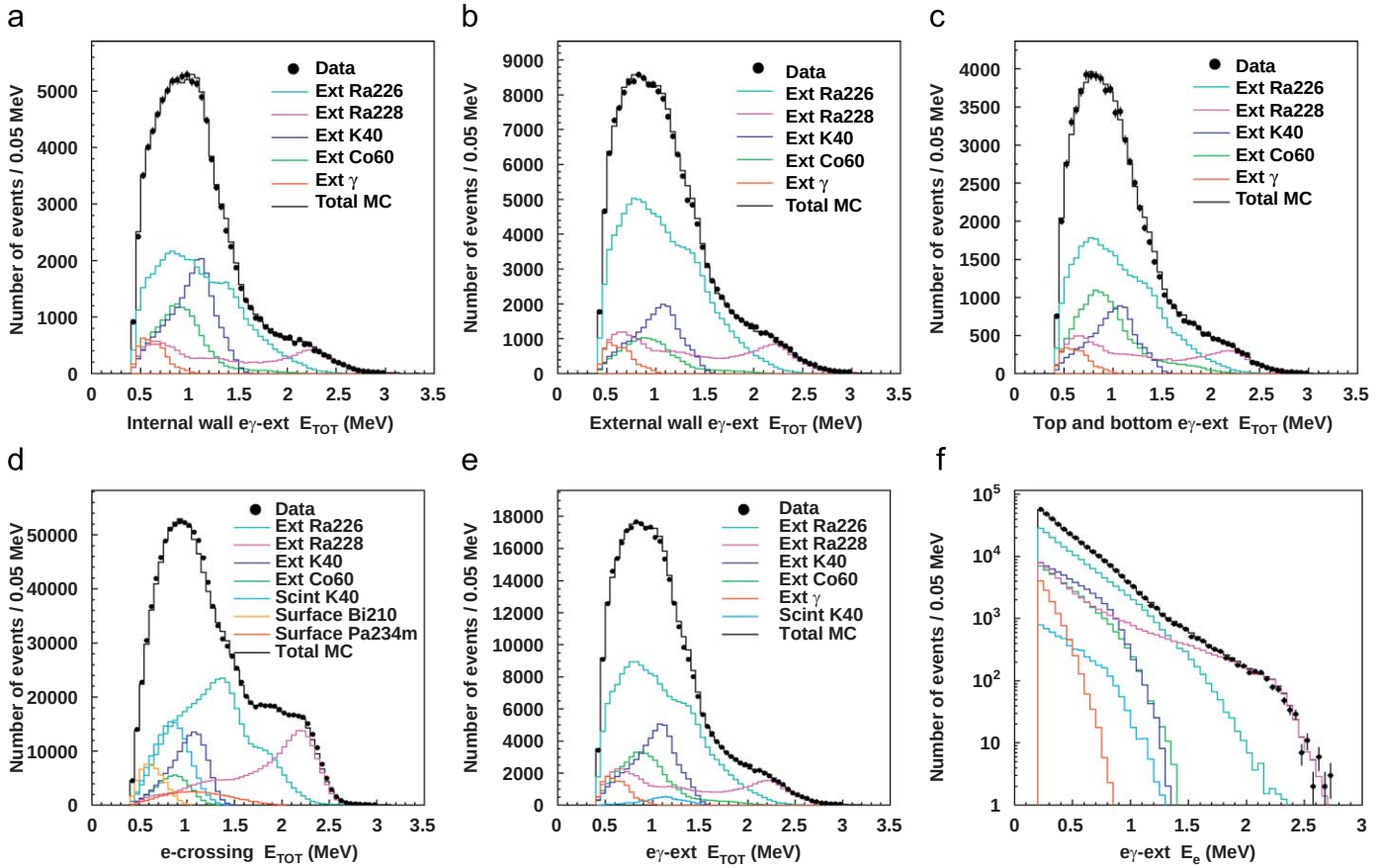

Fig. 15. Results of the fit for the Phase 2 data. The energy sum distribution of eγ-external events with incoming γ-rays detected at (a) the internal wall, (b) the external wall and (c) the end-caps at the top and bottom of the detector. Distributions for the whole detector: (d) energy sum of crossing electron events, (e) energy sum of the electron and γ-ray for eγ-external events and (f) detected electron energy for eγ-external events.

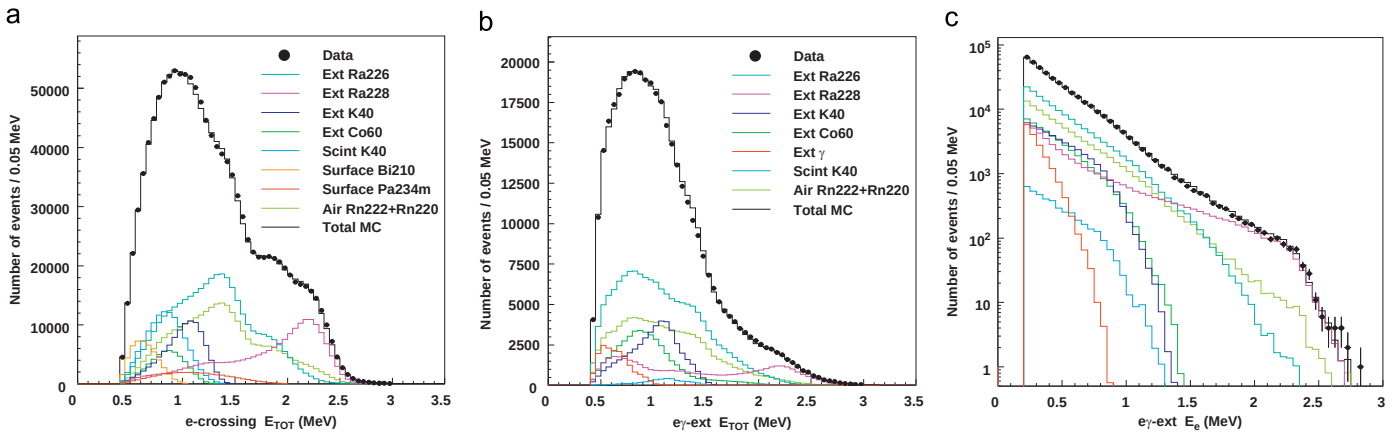

Fig. 16. Results of the fit for the Phase 1 data: (a) energy sum of crossing electron events, (b) the energy sum of the electron and γ-ray for eγ-external events and (c) the detected electron energy for eγ-external events.

from three different productions and their activities were measured with HPGe detectors before foil fabrication. The results of these measurements are given in column A2 of Table 7. After the source foil fabrication the foil activity was again measured. Results are shown in column A4 of Table 7. For most of the measurements only limits could be achieved.

To make the fit the ^{214}Bi activity inside the mylar films covering the foils (ifany) is fixed to the value measured with the HPGe detector. The measurement of the internal ^{214}Bi contamination of each NEMO 3 source material, using this method, is given in column A1 of Table 7. When only a limit on the mylar activity is available two results are given. The first is obtained with the limit value, the second with the mylar activity set to zero.

Column A3 shows the total ^{214}Bi activity of the source foils calculated from the values of columns A1 and A2. When only a limit is known for the mylar contamination by ^{214}Bi there is a systematic uncertainty on the total foil activity reflected by the difference between two numbers in the column A3. When a limit is obtained on the internal foil material activity A1 (the case of ^{130}Te) the first number in column A3 corresponds to A1 = 0, the second is for the limit value of A1. There is a good agreement

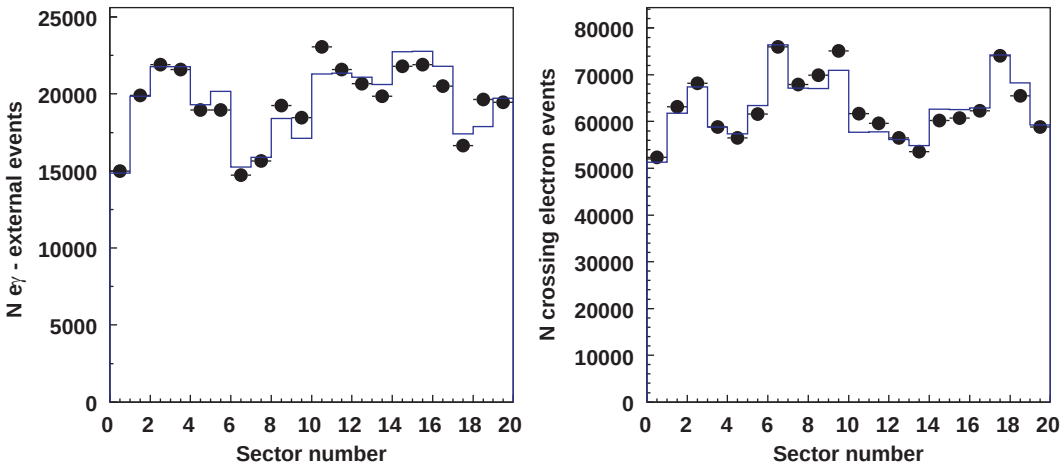

Fig. 17. Two distributions of the number of events per sector (left eγ-external and right crossing electrons). The data are given by black dots and the MC simulations are shown with a solid line.

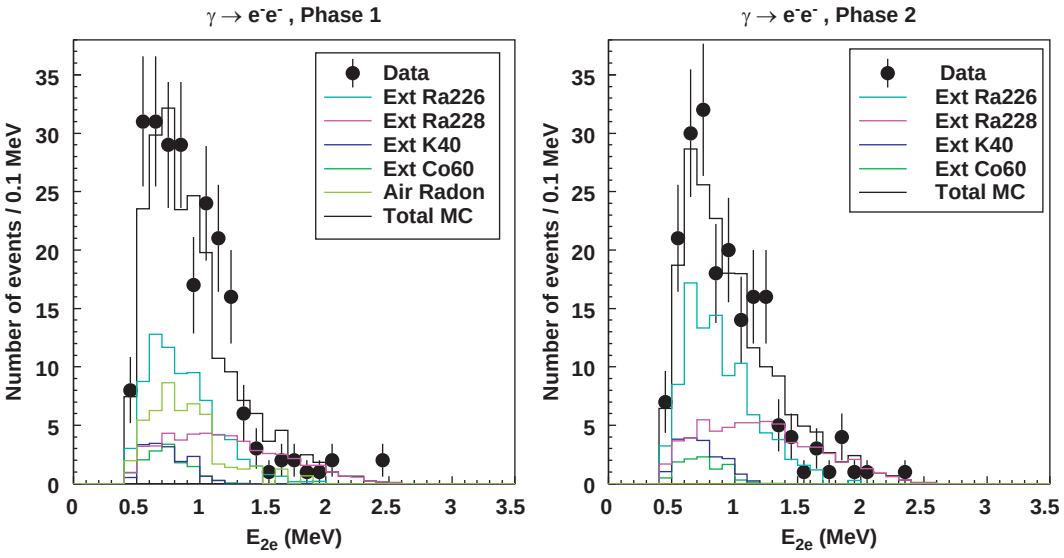

Fig. 18. Energy sum distribution of the two electrons in eeγ-external events compared to the results obtained with the external background model.

between the results obtained from NEMO 3 data and those from the HPGe detectors.

4.2. ^{208}Tl *inside the source foils*

The presence of a small quantity of ^{208}Tl from the ^{232}Th decay chain inside a source foil is the origin of the most troublesome background for the neutrinoless double beta decay search. Therefore, the radiopurity goals of molybdenum and selenium foils were very high [1]. The measurements using HPGe detectors could not reach the required sensitivity and in most cases only limits on ^{208}Tl activity were set. Here the measurements of ^{208}Tl foil contamination performed with NEMO 3 data are presented.

Events of eγγ and eγγγ topologies are used. The event selection criteria are similar to those described in Section 2.2.1 but in this case the event vertex has to be on the source foil. All likely backgrounds have been taken into account. The most important one is due to the thoron and radon in the detector volume. The two event topologies give consistent results and the activities evaluated with Phase 1 and Phase 2 data are in a good agreement. The ^{208}Tl activity in the ββ source foils and in the copper foils based on the total available statistic are presented in Table 8.

The results of HPGe detector measurements are also presented in Table 8 for comparison. With the exception of natural tellurium there exists a good agreement between the two measurements. Due to the large data acquisition time NEMO 3 achieves better sensitivity.

4.3. *Measurement of the internal activity of* β *emitters*

The beta activity of a foil is measured by events with a single electron track. The sources of radioactivity considered above are not sufficient to explain the single electron data. An additional source of electrons in the foils is required. The results of the foil radiopurity measurements performed with HPGe detectors before the foil installation in NEMO 3 are used to decide upon the list of contaminants in a given foil. This list typically includes ^{40}K and isotopes from ^{238}U and ^{232}Th decay chains. The internal ^{226}Ra and ^{228}Ra activities are fixed from the results obtained for ^{214}Bi and ^{208}Tl described above. Their daughters are assumed to be in equilibrium. A possible foil surface pollution by ^{210}Pb is also considered.

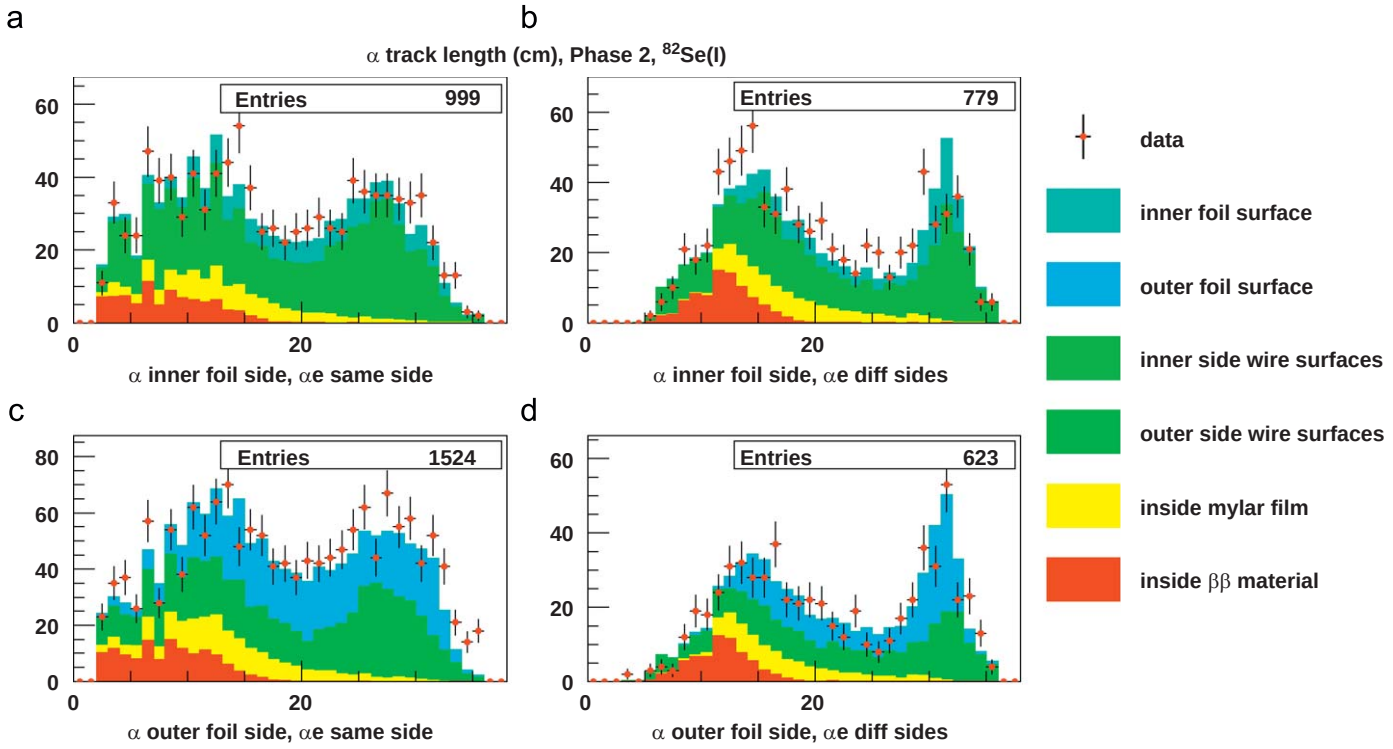

Fig. 19. Delayed track length distributions for the events of Phase 2 with vertices on the selenium source foils is shown by points with error bars. The MC simulations are shown with histograms. The results for events with both the α track and the fast track (e^-) on the same side of the source foil are shown in plots (a) and (c) while those having the α track and the electron on different foil sides are shown in plots (b) and (d).

Table 7
Measurements of ^{214}Bi activity of the source foils, mBq/kg.

Source foil	A1	A2	A3	A4
^{100}Mo(m)	<0.1	–	<0.1	<0.39
^{100}Mo(c)	<0.1; 0.30 ± 0.07	<0.67	<0.15; 0.27 ± 0.07	<0.34
^{82}Se(I)	1.0 ± 0.13	1.7 ± 0.5	1.1 ± 0.17	<4.2
^{82}Se(II)	0.4 ± 0.15	1.7 ± 0.5	0.53 ± 0.18	1.2 ± 0.5*
^{96}Zr	6.4 ± 2.; 7.8 ± 2.	<0.67	5.5 ± 1.7; 6.5 ± 1.7	<16.7
^{150}Nd	2.7 ± 0.4	3.3 ± 0.5	2.8 ± 0.4	<3.3
^{130}Te	<0.1	3.3 ± 0.5	0.39 ± 0.06; 0.48 ± 0.06	<0.67
Te(nat)	0.13 ± 0.1	1.7 ± 0.5	0.28 ± 0.14	<0.17
^{116}Cd	0.6 ± 0.15; 0.67 ± 0.13	<1.0	0.65 ± 0.13; 0.59 ± 0.13	<1.7
Cu	<0.1	–	<0.1	<0.12

A1—results of the fit for the foil activity excluding the contribution from mylar. A2—mylar activity measured with HPGe detectors, A3—total foil activity including mylar calculated from A1 and A2, A4—foil activity measured with HPGe. The following notations are used for different source foil types: ^{100}Mo(m)—for the metallic molybdenum, ^{100}Mo(c)—for the composite molybdenum, ^{82}Se(I)—for the selenium sample of the first enrichment and ^{82}Se(II)—for the second.

*Samples of ^{82}Se(I) and ^{82}Se(II) having a combined mass of 800 g have been measured. The ^{82}Se(II) was not measured separately.

Table 8
Number of observed events (N), signal-to-background ratio (S/B), signal efficiency (ε) and results of the measurements of ^{208}Tl activity of the source foils compared to the HPGe measurements.

ββ material	N	S/B	ε (%)	A (mBq/kg)	A_{HPGe} (mBq/kg)
^{100}Mo(m)	666	2.4	1.7	0.11 ± 0.01	<0.13; <0.1; <0.12*
^{100}Mo(c)	1628	1.7	1.8	0.12 ± 0.01	<0.17
^{82}Se(I)	446	2.0	2.0	0.34 ± 0.05	<0.670
^{82}Se(II)	507	3.4	1.9	0.44 ± 0.04	0.4 ± 0.13**
^{48}Ca	42	4.1	1.4	1.15 ± 0.22	<2.
^{96}Zr	158	7.9	1.8	2.77 ± 0.25	<10.; <5.*
^{150}Nd	1002	39.4	1.8	9.32 ± 0.32	10. ± 1.7
^{130}Te	448	1.1	2.0	0.23 ± 0.05	<0.5
^{nat}Te	495	1.9	1.8	0.27 ± 0.04	<0.08
^{116}Cd	196	0.7	1.7	0.17 ± 0.05	<0.83; <0.5*
Cu	66	0.6	1.5	0.03 ± 0.01	<0.033

*Different foil samples have been measured.

**Samples of ^{82}Se(I) and ^{82}Se(II) having a combined mass of 800 g have been measured. The ^{82}Se(II) was not measured separately.

HPGe measurements made for the copper foils have revealed that the copper is quite clean. Upper limits of 5 and 8 mBq/kg on the contamination by ^{234m}Pa and ^{40}K, respectively were attained. Here the internal activities of these beta emitters are determined by a fit to the single electron energy spectra obtained from Phase 2.

The results of the fit are shown in Fig. 20 demonstrating a good agreement with the data. An activity of 1.5 ± 0.1 mBq/kg is found for ^{234m}Pa and 3.7 ± 0.1 mBq/kg for ^{40}K. No pollution on the copper foil surface by ^{210}Pb was evident. In Fig. 20 the ^{210}Bi contribution corresponds to the wire surface contamination.

The same method provides the determination of the contaminant activities in the ββ source foils. The "single electron" channel is the most appropriate for pure beta emitters. For isotopes decaying with copious γ-ray emission such as ^{60}Co and ^{207}Bi, the eγ-internal channel is used.

5. Test of the background model

The highly radiopure copper foils (621 g) occupy one of the 20 sectors in NEMO 3. They are used to measure the external background. The internal eγ and $2e^-$ channels are used to compare the data with the background model described above.

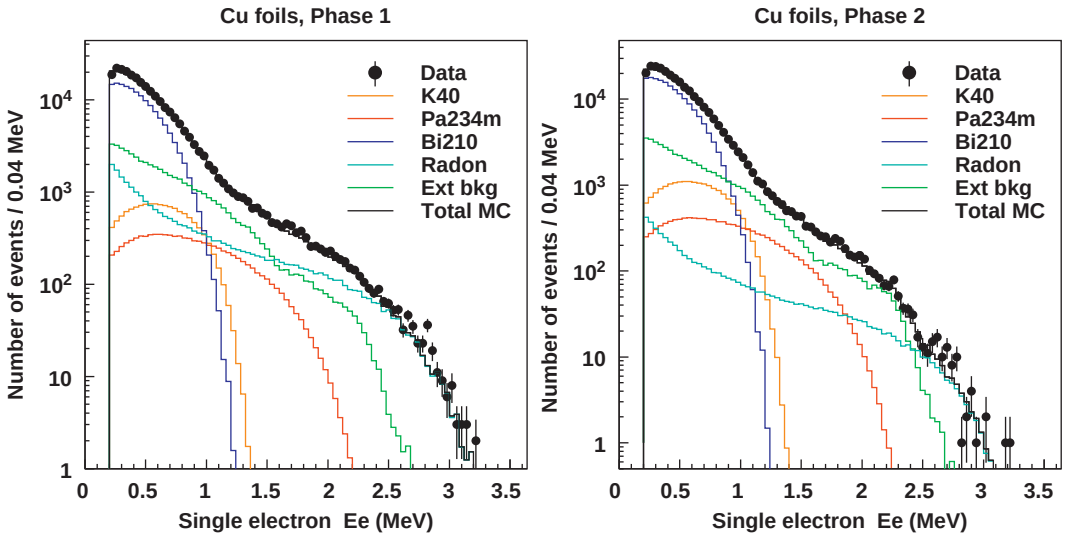

Fig. 20. Single electron energy spectra for copper, Phase 1 and Phase 2 data.

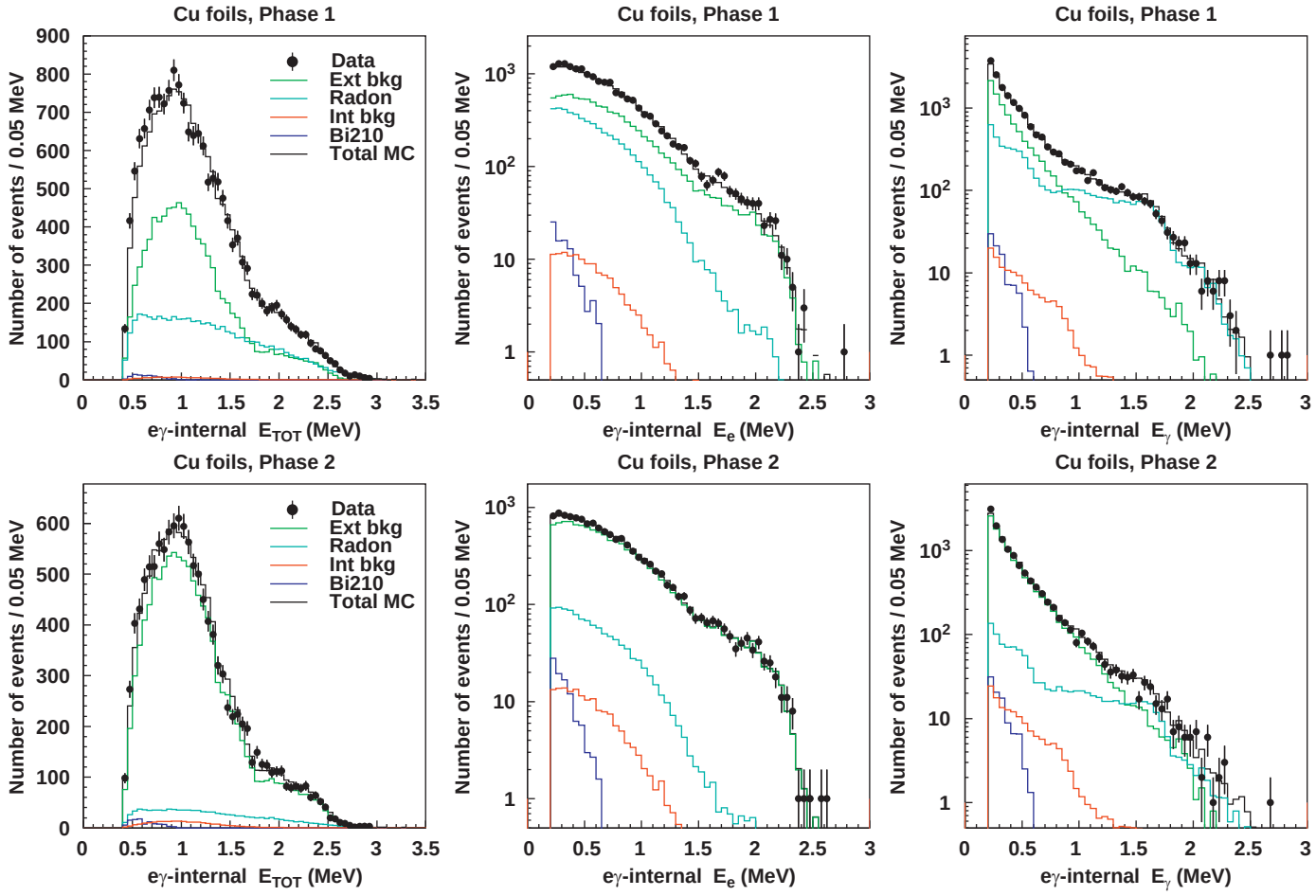

Fig. 21. The distribution of the energy sum of the e^- and γ-ray, the single e^- energy and the single γ-ray energy of internal $e^-\gamma$ events from copper foils for Phase 1 and Phase 2 data.

5.1. *Internal eγ events from the copper foils*

In Fig. 21 some distributions of internal eγ events coming from the copper foils are compared with the MC simulation based on the background model. One can see that the total number of events and the energy spectra are closely reproduced.

The external background is dominant and represents almost 90% of all internal eγ events in Phase 2. In Phase 1 the radon produces a noticeable contribution, and in the energy sum region below 1 MeV there are slightly more events than expected. The difference is less than 2% of the total number of events. In Phase 2 the radon contribution is significantly lower and the model

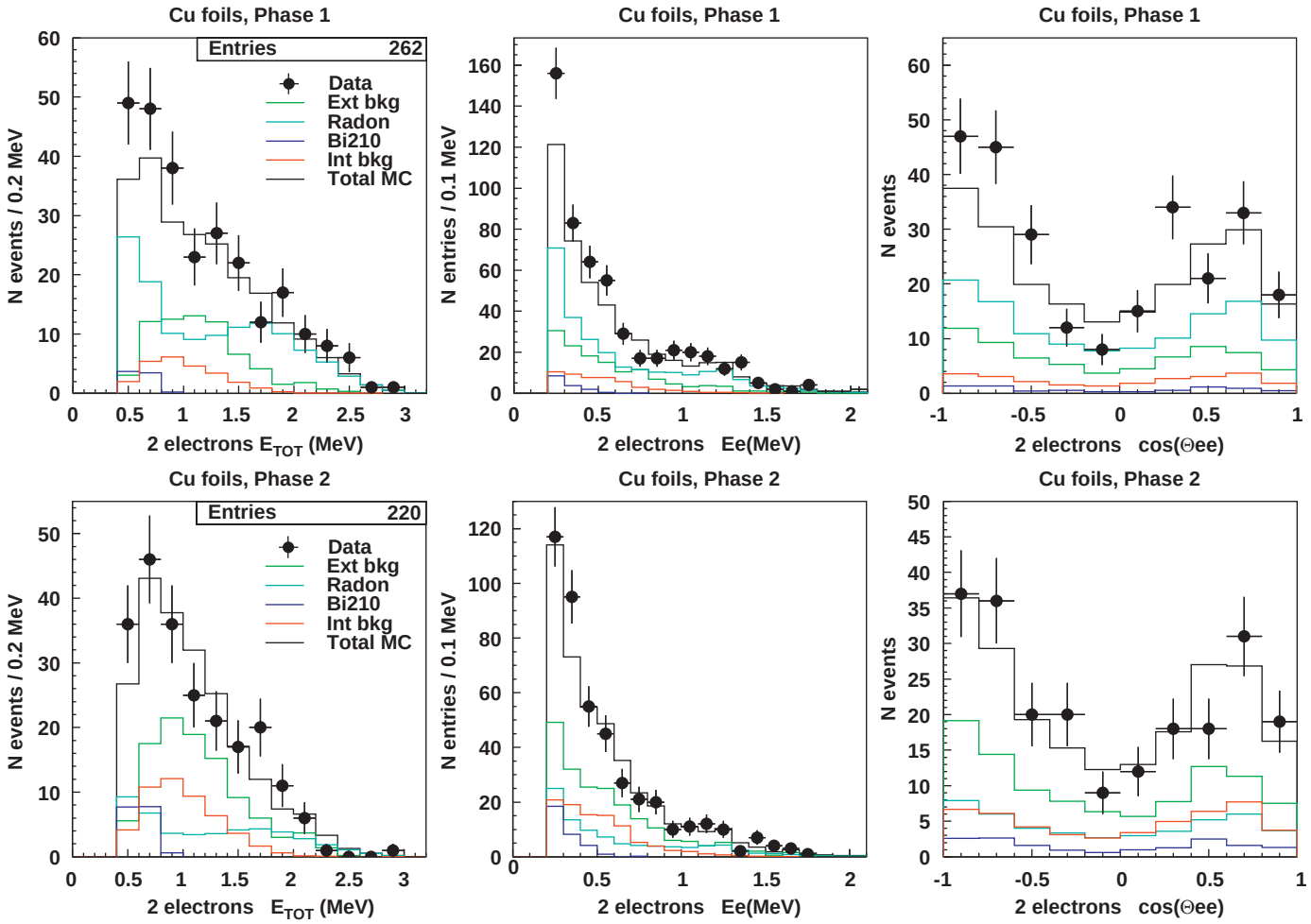

Fig. 22. Background model prediction compared to the data for $2e^-$ events from the copper foils.

describes the data very well even at low energies. A similar problem at low energies for the Phase 1 data is also observed in the $2e^-$ channel and may have the same origin.

The internal background contribution in the $e\gamma$ channel is negligible so the data confirms that the copper foils are clean.

5.2. Two electron events from the copper foils

Copper is not a source of double beta decay. That allows one to check the validity of the background model in the $2e^-$ channel where double beta decay is searched for. To study this channel the events are selected by requiring two reconstructed electron tracks emitted from the foil with the correct curvature and a common vertex in the foil. The energy of each electron measured in the calorimeter is required to be greater than 200 keV. Each track must hit an isolated scintillator block and no additional PMT signals are allowed to avoid events with γ-rays. The event is also recognized as internal by the time-of-flight difference of the two electrons.

In Fig. 22 the distributions of the energy sum of the two electrons, the single electron energies and angular correlation of two-electron events coming from the copper foils are compared to the prediction of the background model. In Phase 2 the total number of events (220 observed with 213 expected for 788 days of data acquisition) have energy and angular distributions in good agreement with the MC predictions. In Phase 1, where the radon activity level is six times higher, there are 262 events observed for the 374 days of acquisition, which is 15% higher than the MC prediction. The excess of events is observed in the energy sum distribution below 1 MeV. The difference is relatively small and is apparently due to radon.

The radon contribution is provided by ^{214}Pb ($Q_\beta = 1.023$ MeV) and ^{214}Bi ($Q_\beta = 3.272$ MeV) decays simulated according to the model based on Ref. [14]. The observed discrepancy at low energies seems to indicate some imperfection in the model for ^{214}Pb and can be due to the shape of the beta spectra. Shapes of beta spectra corresponding to allowed decays were generated, while the beta transitions are mainly of the first non unique forbidden type. A deviation from the allowed shape for this type of transition may be large [19,20], however it is not known for ^{214}Pb and ^{214}Bi.

Apart from the problem at low energies in Phase 1 the background model successfully reproduces the $2e^-$ events produced in the copper foils due to the external and internal radioactive sources.

6. Summary

The methods of background measurements in the double beta decay experiment NEMO 3 are presented. The background is classified as internal and external according to its origin. Internal backgrounds come from the source foils. The external background is subdivided into two groups. The first is due to radioactive sources inside the tracking volume, and the second results from the radioactivity outside of the tracking volume. All these

backgrounds were estimated from the data with events of various topologies as summarized below.

- The external background component due to the presence of radon in the tracking chamber is measured using events with a detected electron accompanied by a delayed α-particle track. This topology results from the beta decay of ^{214}Bi followed by the alpha decay of ^{214}Po.
- The thoron is measurable with the events of $e\gamma\gamma$ and $e\gamma\gamma\gamma$ topologies. The method is based on the detection of events with the signal of a 2.615 MeV γ-ray, typical of the ^{208}Tl beta decay.
- The presence of ^{210}Pb on the wires is measured with a single electron starting from a wire.
- The external γ-ray flux coming from outside of the tracking detector volume is measured with a crossing electron and $e\gamma$-external events.
- The internal background due to ^{214}Bi and ^{208}Tl decays inside the foil is measured in a manner similar to that used for radon and thoron measurements but requires the event vertex to be located on the foil.
- The use of single electron events without detected γ-rays and coming from a source foil allows one to measure the activity of beta emitters inside the foils.

Very pure copper foils are used for the study of the external background with internal $e\gamma$ events. The validity of the background model is successfully verified with $2e^-$ events coming from the copper foils.

It has been demonstrated that with the NEMO 3 detector the backgrounds are measurable from the experimental data. In particular the activities of the two most troublesome background sources for $\beta\beta0\nu$ decay, ^{214}Bi and ^{208}Tl, are measured with the adequate precision.

Acknowledgments

The authors would like to thank the Modane Underground Laboratory staff for their technical assistance in running the experiment. Portions of this work were supported by Grants from RFBR (nos. 06-02-16672 and 06-02-72553) and by the Russian Federal Agency for Atomic Energy. We acknowledge support by the Grant Agencies of the Czech Republic (MSM 6840770029, LA305 and LC07050).

References

[1] R. Arnold, et al., NEMO Collaboration, Nucl. Instr. and Meth. A 536 (2005) 79.
[2] R. Arnold, et al., NEMO Collaboration, Phys. Rev. Lett. 95 (2005) 182302.
[3] R. Arnold, et al., NEMO Collaboration, Nucl. Phys. A 765 (2006) 483.
[4] R. Arnold, et al., NEMO Collaboration, Nucl. Phys. A 781 (2007) 209.
[5] R.B. Firestone, et al., Table of Isotopes, 8th ed., Wiley, NY, 1998.
[6] G. Frey, P.K. Hoke, J.J. Stukel, Science 211 (1981) 480.
[7] A. Busigin, et al., Health Phys. 40 (1981) 333.
[8] E.M. Wellisch, Philos. Mag. 26 (1913) 623.
[9] A. Renoux, Etudes des ions radioactifs de l'atmosphère, thèse de doctorat, Université de Fac-Science, Rapport CEA R-2771, Paris, France, 1965.
[10] J. Porstendörfer, T.T. Mercer, Health Phys. 37 (1979) 191.
[11] R. Arnold, V.I. Tretyak, The NEMO 3 simulation program, NEMO 3 internal note IReS-1/97, Strasbourg, 1997.
[12] GEANT Detector Description and Simulation Tool, CERN Program Library Long Writeup W5013 ⟨http://wwwasdoc.web.cern.ch/wwwasdoc/geant_html3/geantall.html⟩, 1995.
[13] O.A. Ponkratenko, V.I. Tretyak, Yu.G. Zdesenko, Phys. Atom. Nucl. 63 (2000) 1282.
[14] Y.A. Akovali, Nucl. Data Sheets 76 (1995) 127.
[15] H. Ohsumi, et al., NEMO Collaboration, Nucl. Instr. and Meth. A 482 (2002) 832.
[16] C. Arpesella, Nucl. Phys. B (Proc. Suppl.) 28A (1992) 420.
[17] Ch. Marquet, et al., NEMO Collaboration, Nucl. Instr. and Meth. A 457 (2001) 487.
[18] V. Chasal, et al., Astroparticle Phys. 9 (1998) 163.
[19] M.M. Be, et al., Proceedings of the International Conference on Advances in Liquid Scintillation Spectrometry, Katowice, 17–21 October 2005.
[20] H. Behrens, L. Szybisz, Phys. Data 6–1 (1976).